# Identification of Dynamic Modes in an Intrinsically Disordered Protein Using Temperature-Dependent NMR Relaxation

Anton Abyzov,[‡] Nicola Salvi,[‡] Robert Schneider,[†] Damien Maurin, Rob W.H. Ruigrok, Malene Ringkjøbing Jensen, and Martin Blackledge*

Institut de Biologie Structurale (IBS), CEA, CNRS, Université Grenoble Alpes, 38044 Grenoble, France

S *Supporting Information*

ABSTRACT: The dynamic modes and time scales sampled by intrinsically disordered proteins (IDPs) define their function. Nuclear magnetic resonance (NMR) spin relaxation is probably the most powerful tool for investigating these motions delivering site-specific descriptions of conformational fluctuations from throughout the molecule. Despite the abundance of experimental measurement of relaxation in IDPs, the physical origin of the measured relaxation rates remains poorly understood. Here we measure an extensive range of auto- and cross-correlated spin relaxation rates at multiple magnetic field strengths on the C-terminal domain of the nucleoprotein of Sendai virus, over a large range of temperatures (268−298 K), and combine these data to describe the dynamic behavior of this archetypal IDP. An Arrhenius-type relationship is used to simultaneously analyze up to 61 relaxation rates per amino acid over the entire temperature range, allowing the measurement of local activation energies along the chain, and the assignment of physically distinct dynamic modes. Fast ($\tau \leq 50$ ps) components report on librational motions, a dominant mode occurs on time scales around 1 ns, apparently reporting on backbone sampling within Ramachandran substates, while a slower component (5−25 ns) reports on segmental dynamics dominated by the chain-like nature of the protein. Extending the study to three protein constructs of different lengths (59, 81, and 124 amino acids) substantiates the assignment of these contributions. The analysis is shown to be remarkably robust, accurately predicting a broad range of relaxation data measured at different magnetic field strengths and temperatures. The ability to delineate intrinsic modes and time scales from NMR spin relaxation will improve our understanding of the behavior and function of IDPs, adding a new and essential dimension to the description of this biologically important and ubiquitous class of proteins.
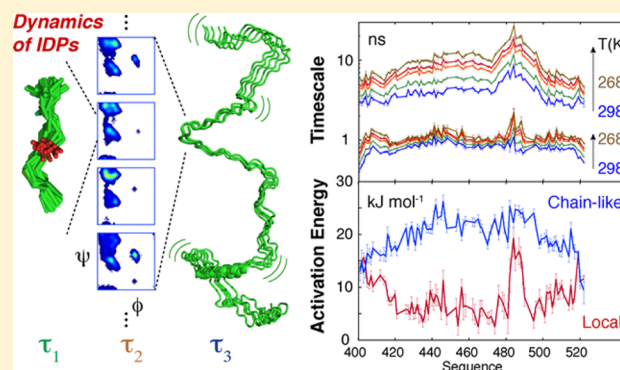
INTRODUCTION

A significantly high proportion of genomes from all domains of life is predicted to code for proteins that are disordered in their functional state.[1−3] The role of the primary sequence of such intrinsically disordered proteins (IDPs) is not to ensure an energetically stable three-dimensional conformation, as in the case of many folded proteins, but rather to sample a continuum of very different conformations on a broad, flat free-energy surface. The observation of such high levels of functionally important disorder has motivated considerable interest in understanding the link between primary sequence composition, the nature of the Boltzmann ensemble sampled at equilibrium, and eventually biological function. Nuclear magnetic resonance (NMR) spectroscopy offers a particularly powerful set of tools for the atomic resolution characterization of disordered proteins in solution, providing population-weighted averages over all conformations present in the ensemble.[4−7] Chemical shifts, and scalar and dipolar couplings average on time scales faster than 100 μs and can be used to describe the conformational space spanned by the conformational ensem-

ble.[8−17] Crucially, however, little is known about the time scales of the intrinsic dynamics of IDPs.

This lack of information about dynamic time scales is important for a number of reasons. The flexible nature of IDPs strongly suggests that their activity is related to their dynamic behavior, in terms of both time scales of motions and extent of conformational excursions. These descriptors define the conformational behavior of the protein and are necessarily correlated with its function. Therefore, our limited understanding of IDP dynamics, even in the free state, is reflected in the limited understanding of their functional mechanisms. Many theoretical and experimental studies have proposed correlations between intrinsic conformational propensities in free and bound states of IDPs, invoking for example conformational selection from the free-state ensemble, or induced fit, as key binding mechanisms.[18−26] Such considerations however tend to ignore intrinsic interconversion rates between free-state backbone conformations, which may

influence molecular association. Similarly, chain-like dynamics will be expected to affect the efficiency of transient secondary interactions, for example via fly-casting mechanisms.[27] Finally, although in principle molecular dynamics (MD) simulation can provide detailed insight into the conformational dynamics of IDPs,[8,28−30] current force fields generally fail to reproduce their macroscopic properties in solution, probably due to the increased importance of protein−solvent interactions.[31−34] The experimental characterization of dynamic time scales is therefore essential for the conception and improvement of force fields that can simulate the behavior of IDPs.

^{15}N spin relaxation[35] offers probably the most powerful and generally accessible tool for the study of the dynamics of IDPs, providing sensitive probes of the motional properties of bond vectors throughout the protein.[36−54] Not surprisingly, spin relaxation is regularly measured, in both free and bound forms of IDPs, and under increasingly relevant physiologically conditions. The presence of segmental motions has been evoked on the basis of the commonly observed bell-shaped dependence of transverse relaxation components, with modulations along the sequence interpreted as a measure of residual order,[36,39,55] for example due to local hydrophobicity,[36,40,45,48,56] or electrostatics.[57,48] Segmental motions in α-synuclein have been proposed on the basis of global ^{1}H relaxometry measurements,[58] while solvent-induced "drag" of long disordered chains has been predicted to affect rotational diffusion properties of partially folded proteins.[59−61] However, despite the abundance of NMR relaxation studies, the physical origin of the measured relaxation rates remains poorly delineated. The aim of this study is to investigate the molecular origin of spin relaxation rates measured in IDPs and, equally importantly, to provide new physical insight into the molecular behavior of IDPs in terms of these essential conformational modes.

In order to achieve this we study the dynamic behavior of the C-terminal domain of the nucleoprotein (NT) of Sendai virus (SeV), a 124 amino acid archetypal IDP, comprising long, unfolded domains and a short molecular recognition motif that interacts with the PX domain of the phosphoprotein.[62,63] Auto- and cross-correlated spin relaxation rates are measured at four magnetic field strengths (600 to 950 MHz ^{1}H frequency) over a large range of temperatures (268−298 K). Up to 61 relaxation rates per site are simultaneously analyzed using an Arrhenius-type relationship relating dynamic time scales over the range of temperatures,[64] allowing assignment of local activation energies of distinct modes along the chain, and identification of the physical origin of the different motional contributions. A fast ($\tau \leq 50$ ps) component reports on librational motions, local backbone sampling of the peptide chain occurs on time scales in the nanosecond range, while the slowest component reports on segmental dynamics dominated by the chain-like nature of the protein. Extending the study to constructs that vary the chain dimensions significantly, supports the assignment of these dominant modes.

■ THEORETICAL CONSIDERATIONS

The five measured relaxation rates are given by the following functions:[35]

$$R_1 = \frac{1}{10}\left(\frac{\mu_0 \hbar \gamma_H \gamma_N}{4\pi r_{NH}^3}\right)^2 (J(\omega_H - \omega_N) + 3J(\omega_N)$$
$$+ 6J(\omega_H + \omega_N)) + \frac{2}{15}\omega_N^2(\sigma_\parallel - \sigma_\perp)^2 J(\omega_N) \quad (1)$$

$$R_2 = \frac{1}{20}\left(\frac{\mu_0 \hbar \gamma_H \gamma_N}{4\pi r_{NH}^3}\right)^2 (4J(0) + J(\omega_H - \omega_N) + 3J(\omega_N)$$
$$+ 6J(\omega_H + \omega_N) + 6J(\omega_H)) + \frac{1}{45}\omega_N^2(\sigma_\parallel - \sigma_\perp)^2$$
$$(4J(0) + 3J(\omega_N)) \quad (2)$$

$$\sigma_{NH} = \frac{1}{10}\left(\frac{\mu_0 \hbar \gamma_H \gamma_N}{4\pi r_{NH}^3}\right)^2 (6J(\omega_H + \omega_N) - J(\omega_H - \omega_N)) \quad (3)$$

$$\eta_{xy} = \frac{1}{15}P_2(\cos\theta)\left(\frac{\mu_0 \hbar \gamma_H \gamma_N}{4\pi r_{NH}^3}\right)(\sigma_\parallel - \sigma_\perp)\omega_N$$
$$(4J(0) + 3J(\omega_N)) \quad (4)$$

$$\eta_z = \frac{1}{15}P_2(\cos\theta)\left(\frac{\mu_0 \hbar \gamma_H \gamma_N}{4\pi r_{NH}^3}\right)(\sigma_\parallel - \sigma_\perp)\omega_N(6J(\omega_N)) \quad (5)$$

where $J(\omega)$ is the angular spectral density function at frequency ω, and θ is the angle between the principal axis of the chemical shift anisotropy (CSA) tensor (assumed axially symmetric with anisotropy $\sigma_\parallel - \sigma_\perp = -172$ ppm) and the N−H dipole−dipole interaction. r_{NH} is the N−H internuclear distance (assumed to be 1.02 Å), γ_H and γ_N are the gyromagnetic ratio of ^{1}H and ^{15}N nuclei respectively, μ_0 is the permittivity of free space, and $\hbar$ is Planck's constant divided by 2π.

The spectral density function of each relaxation-active vector in highly disordered systems can be mapped by solving for the different characteristic $J(\omega)$ contributing to the different relaxation rates.[65] Reduced spectral density mapping[66−68] is often used to determine $J(0)$, $J(\omega_N)$, and $J(0.87\omega_H)$, where the latter is an effective value representing J at higher frequencies.

In folded proteins, relaxation rates are commonly interpreted using the model-free approach, where contributions from local and global motions to the autocorrelation function are analytically separated,[69−72] the latter being treated as a common contribution for all sites. The concept of common overall motion has little relevance for IDPs, prompting the development of alternative approaches, evoking either a distribution of correlation times[41,44,51,73] or MD-based frameworks for identifying relaxation-active correlation times.[74] Alternatively, the model-free approach can be applied in a general form for each site, with different contributions to the correlation function/spectral density function representing independent motions occurring on distinct time scales. Modeling the distribution of motions with a limited number of contributions (normally two or three) surely oversimplifies the large number of possible modes, but nevertheless provides valuable insight into the variation of dynamic behavior along the chain.[75,76]

As noted by Halle,[72] provided that the time scales are sufficiently separated, the adiabatic approximation holds and, assuming all motions to be isotropic, the correlation function $C(t)$ can be modeled by the sum of exponentially decaying terms:
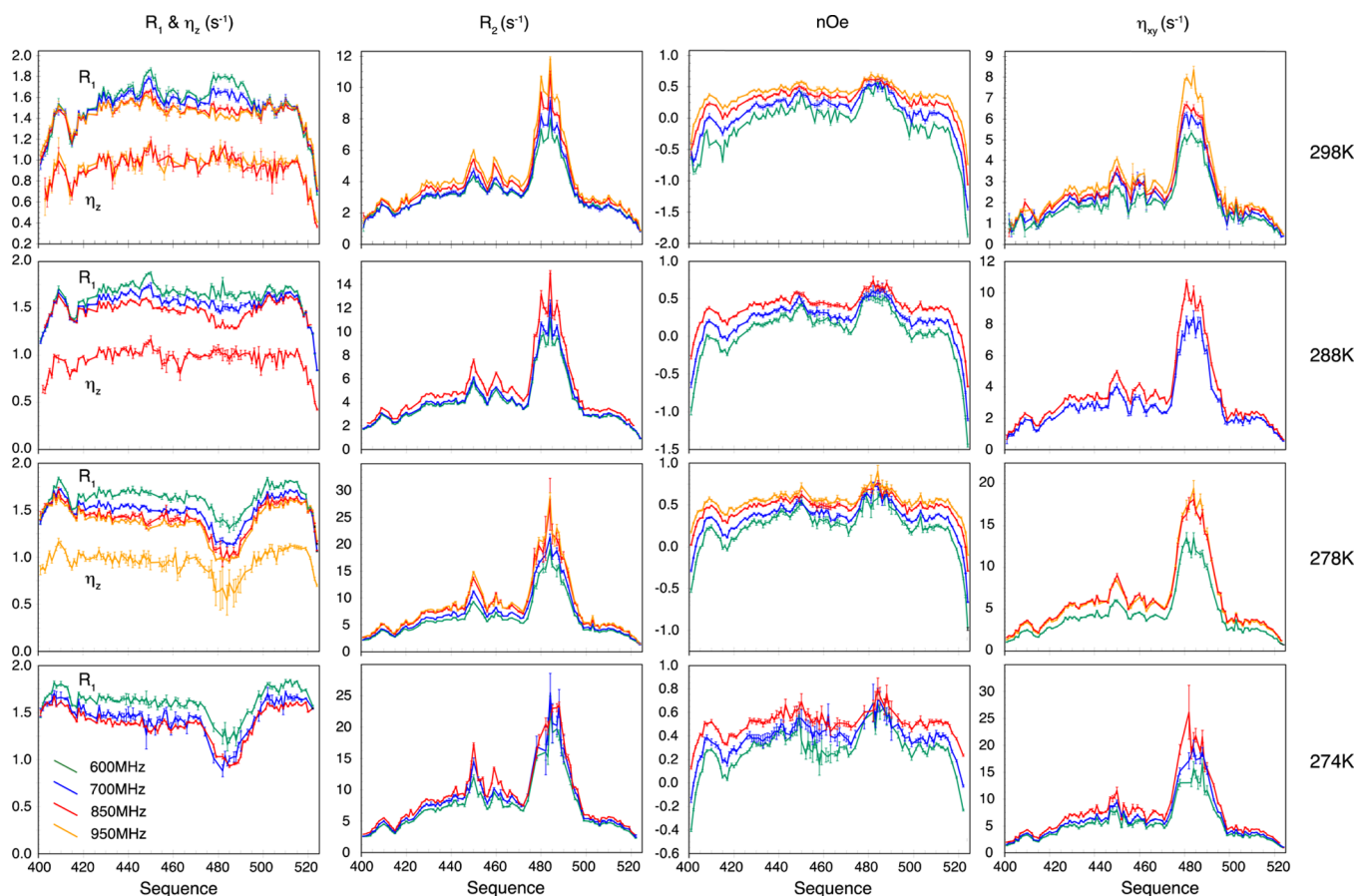
Figure 1. Experimental relaxation rates of NT_L (residues 401−524), measured at different magnetic field strengths (green, 600 MHz ^1H frequency; blue, 700 MHz; red, 850 MHz; orange, 950 MHz) and temperatures (top row, 298 K; second row, 288 K; third row, 278 K; bottom row, 274 K). Longitudinal relaxation R_1 and η_z are shown in the same panels; in this case, the lower curves correspond to the cross-correlated relaxation rates. Data were also measured at 268 K (Supporting Information Figure S2).

$$C(t) = \sum_k A_k e^{-t/\tau_k} \tag{6}$$

The requirement of separation of time scales implies that faster contributions decay completely before the slower contributions significantly affect the correlation function (Figure S1). The definition of the amplitudes A_k implies that $\sum_k A_k = 1$.

The Fourier transformation of $C(t)$ yields the spectral density function

$$J(\omega) = \sum_k \frac{A_k \tau_k}{1 + \omega^2 \tau_k^2} \tag{7}$$

In this study, we use an Arrhenius analysis to relate individual dynamic contributions at different temperatures via the following function:

$$\tau_k(T) = \tau_{k,\infty} e^{E_{k,a}/RT} \tag{8}$$

where $E_{k,a}$ represents the local activation energy (Gibbs free energy or free enthalpy) of the process k associated with the different components, and $\tau_{k,\infty}$, the prefactor that represents the correlation time at infinite temperature. This approach allows us to simultaneously analyze relaxation rates measured at multiple fields and temperatures to extract local activation energies, while at the same time increasing the robustness of the fitting procedure involving multiple time scales.

RESULTS

Site-Specific Dynamics of Intrinsically Disordered NT As a Function of Temperature. Longitudinal and transverse auto- and cross-correlated ^{15}N relaxation rates were measured at 600, 700, 850, and 950 MHz (^1H frequency) from NT at four different temperatures (Figure 1). Relaxation rates were also collected at 268 K at 600 MHz (Figure S2). Distinct conformational properties of different regions of the protein are immediately discernible. The helical element (476−492) exhibits relaxation rates typical of slower correlation times, with additional local structure apparent around two tryptophans at positions 443 and 451, while a clear dip appears in most relaxation rates around residue 415, indicative of increased flexibility coincident with three consecutive glycine residues. The temperature dependence of the different rates is more explicitly shown in Figure 2 for experiments performed at 850 MHz.

Reduced spectral density mapping was performed for data obtained at each magnetic field strength and at each individual temperature. Comparison of $J(0)$ derived from analysis of relaxation data from different field strengths using autocorrelated relaxation rates (R_1, R_2, and σ_{NH}) and cross-correlated rates (η_{xy}, η_z) indicates that exchange contributions to R_2 are negligible and reveals a high level of consistency between the different data sets (Figure S3). Cross-correlated transverse relaxation rates exhibit similar periodicity along the helical element as residual dipolar couplings (RDCs) measured in NT
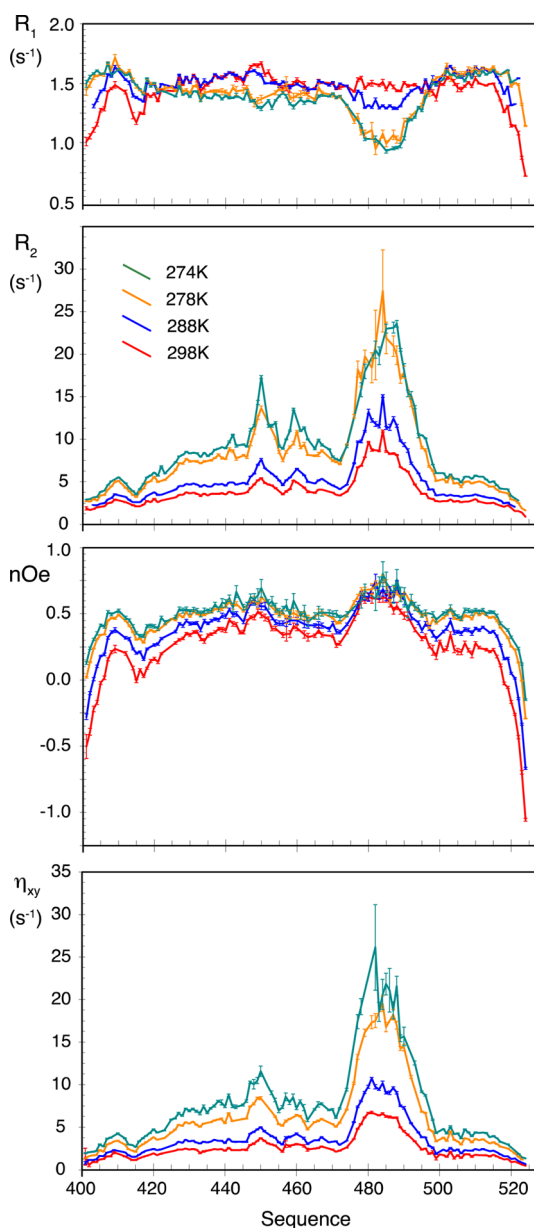
Figure 2. Experimental relaxation rates (R_1, R_2, NOE, and η_{xy}) of NT_L (residues 401−524), measured at 850 MHz ^1H frequency (green, 274 K; orange, 278 K; blue, 288 K; red, 298 K).

Figure 3. Sequence dependence of the correlation time of the fast (τ_1), intermediate (τ_2), and slow (τ_3) correlation times in NT_L for a three-exponential model of the autocorrelation function using the model-free approach with the fast motional time scale as a free parameter, except in the helix where τ_1 is set to 0. Analysis is shown for data measured at 298 K (red), 288 K (blue), 278 K (orange), and 274 K (green). The dashed line indicates a value of 50 ps. No obvious progression of the fast component is seen as a function of temperature. The y-axis is shown on a logarithmic scale.

(Figure S4), which report on distinct helical substates in fast exchange.[77,78] Anisotropic rotational diffusion induces similar orientational dependence in ^{15}N relaxation rates as steric alignment induces in dipolar couplings.[79] Although the time scale of interconversion of the helical substates is unknown, this similar periodicity is consistent with exchange time scales that are too slow to be relaxation-active (but fast on the chemical shift time scale). Our subsequent analysis assumes that the measured rates therefore report on averages over relaxation occurring in each helical state.

We note that the backbone conformational propensities remain stable with temperature in the unfolded regions of NT, while the predominantly helical region (residues 476−492) shows a slight increase in helical propensity (around 5−7%) at lower temperatures as judged from temperature-corrected[80] $^{13}C^\alpha$ chemical shifts (Figure S5).
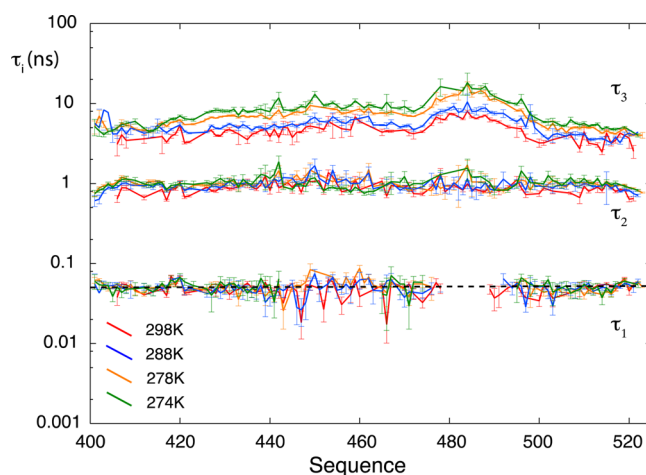
Identification of Appropriate Dynamic Models of the Spectral Density Function.

Data measured at 274, 278, 288, and 298 K were independently analyzed by minimizing eq 10, assuming one, two, or three exponential contributions to auto- and cross-correlation functions (eqs 6,7). Statistical analysis (Figure S6) is consistent with the use of a six-parameter (A_2, A_3, τ_1, τ_2, τ_3, and θ) model throughout the protein and a five-parameter (A_2, A_3, τ_2, τ_3, and θ with $\tau_1 = 0$) model in the helix (residues 476 to 492). The time scales of the three different contributions resulting from this analysis are shown in Figure 3 for the four temperatures (274, 278, 288, and 298 K) for which (12, 14, 14, and 18) different relaxation rates were measured, respectively. Outside the helical region, the faster time scale motion is closely distributed around 50 ps at all four temperatures. Indeed fixing this component to 50 ps has negligible impact on the motional amplitudes (Figures 4 and S7).

The slower time scale motion varies through a range from around 5 to 25 ns over the whole temperature range, with clear maxima in the helical region, while the intermediate time scale motion ranges from 0.5 to 1.3 ns. Not surprisingly the relative contribution of the slowest component increases as temperature drops, with a concomitant reduction in the faster component, in particular in the helical element. In order to investigate these effects in more detail we have analyzed data from all four temperatures simultaneously (vide infra). The derived site-specific dipole−dipole/CSA interaction angle θ corresponds to an effective value reproducing the ensemble-averaged $P_2(\cos\theta) = \frac{3\cos^2\theta - 1}{2}$ in eqs 4 and 5, which may absorb a number of effects, for example local anisotropies that are not accounted for in our analysis. θ values derived at 298, 288, and 278 K generally fluctuate around 22°−25° in the unfolded region (Figure S8), with lower values occurring in the helical region, in line with studies of folded proteins.[81−83] Repeating the analysis with fixed values of θ (22°) results in essentially identical motional parameters, inducing small
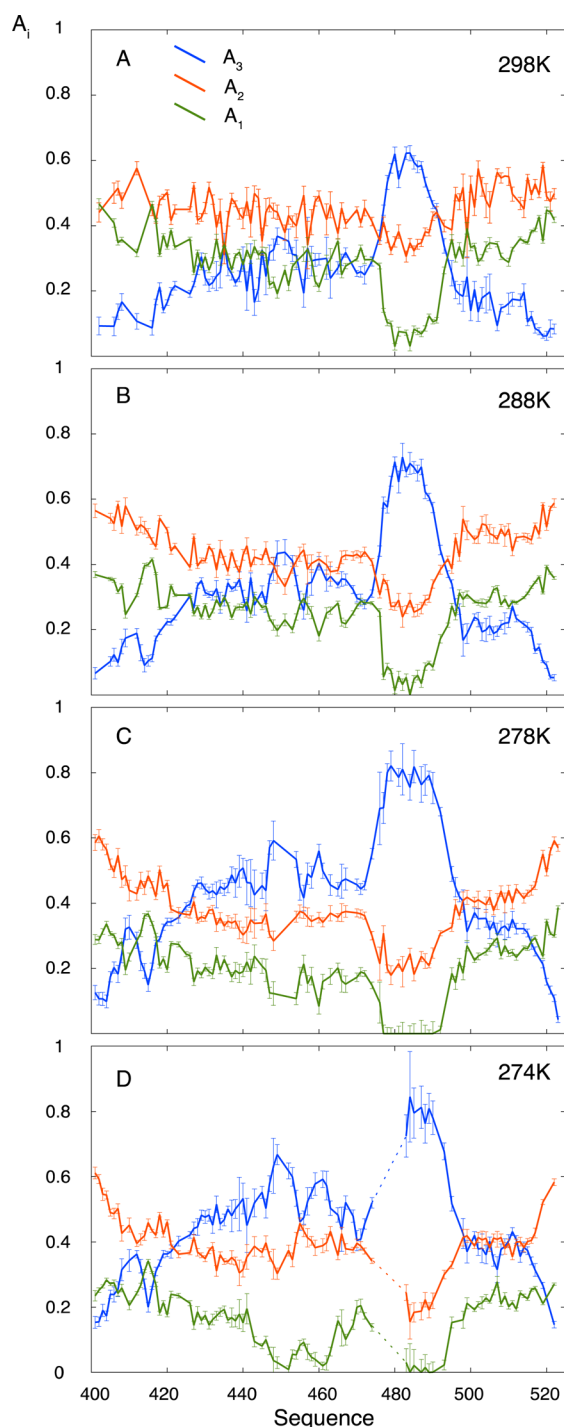
Figure 4. Amplitude of the motional contributions A_1 (fast contribution, shown in green), A_2 (intermediate time scale contribution, shown in orange), and A_3 (slowest contribution, shown in blue) in NT_L at the four temperatures, 298 K (A), 288 K (B), 278 K (C), and 274 K (D). The fast component clearly falls in amplitude with decreasing temperature, while the slow contribution increases. The dashed line in Figure D corresponds to residues for which insufficient data were available to characterize the dynamics with sufficient accuracy.

discrepancies between predicted and calculated η_{xy} and R_2 values. No correlation was found between θ and the motional parameters A_i and τ_i. The combined analysis of data at multiple

temperatures assumes a single value for θ for each site across all temperatures.

Site-Specific Temperature Dependence of the Spectral Density Function. All data from all temperatures were fitted using a single function with three motional components, characterizing intermediate and slow time scale motions with Arrhenius-type dependences for each site (see Theoretical Considerations). This requires the determination of $\tau_{2,\infty}$, $\tau_{3,\infty}$, $E_{2,a}$, and $E_{3,a}$ where 2 and 3 refer to the two components respectively, θ for each site, and A_2, A_3 for each temperature. The fast time scale motion, which shows negligible temperature dependence (see above), was fixed to 50 ps throughout the protein and 0 ps in the helical region at all temperatures. A total of 58 relaxation rates were fitted to these 13 parameters for 86 resonances that were resolved at all temperatures. The results are summarized in Figure 5, with data reproduction shown in Figure S9. θ values show a smooth distribution along the primary sequence with limited variance ($23.5 \pm 2.5°$) and lower tendencies in the helical region (Figure S10).

The time scale of the slower contribution exhibits a distinct bell-shaped distribution, while the intermediate time scale is overall flatter, with deviations to slower time scales in the helical region. The steeper temperature dependence of the slower time scale motion is reflected in the higher effective activation energy (reaching $20-25$ kJ mol^{-1} in the center of the chain) compared to the intermediate time scale motion. The activation energy of the slower time scale motion also exhibits a broad bell-shaped sequence dependence, encompassing the helical region with only a minor increase in the range 476–492, while the intermediate motion in the region 425–500 shows a flatter distribution (around 5 kJ mol^{-1}) that is clearly interrupted by the helical element, where activation energies are locally increased to 15 kJ mol^{-1}. Motional amplitudes are very similar to those determined from the individual temperature analysis. Interestingly the intermediate time scale motion has a maximum contribution at 288 K. Although only three rates could be accurately measured at 268 K, the five-temperature Arrhenius analysis (determination of 15 parameters from 61 relaxation rates) is fully consistent with the four-temperature analysis, resulting in very similar trends for A_1, A_2 and A_3 as well as τ_2 and τ_3 (Figure S11).

We note that the temperature dependence of tabulated values of the viscosity for 500 mM NaCl solution[84] compare closely with the observed temperature dependence of the time scale of the slow component (Supporting Information Figure S12). The effective temperature coefficient is predicted to be 20.5 kJ mol^{-1}, suggesting that the slower component detected in the relaxation rates is dominated by solvent viscosity. Intermediate motions, whose activation energy is much lower than the solvent-dominated temperature coefficient, are more convincingly associated with internal modes.

Robustness of the Analysis. In order to determine the robustness of this analysis we have performed the following cross-validations: 10% of all experimental data were randomly removed, and the analysis was repeated in the absence of these "passive" data points, whose values were predicted on the basis of the analysis of the active data. The results, shown in Figure 6A for three separate random selections, give a remarkably good reproduction of the passive data (Pearson's correlation coefficient $r > 0.995$). An additional plot showing the close reproduction of the rates across the sequence is included in the Supporting Information (Figure S13). Second, we have tested the dependence of the analysis on available magnetic field
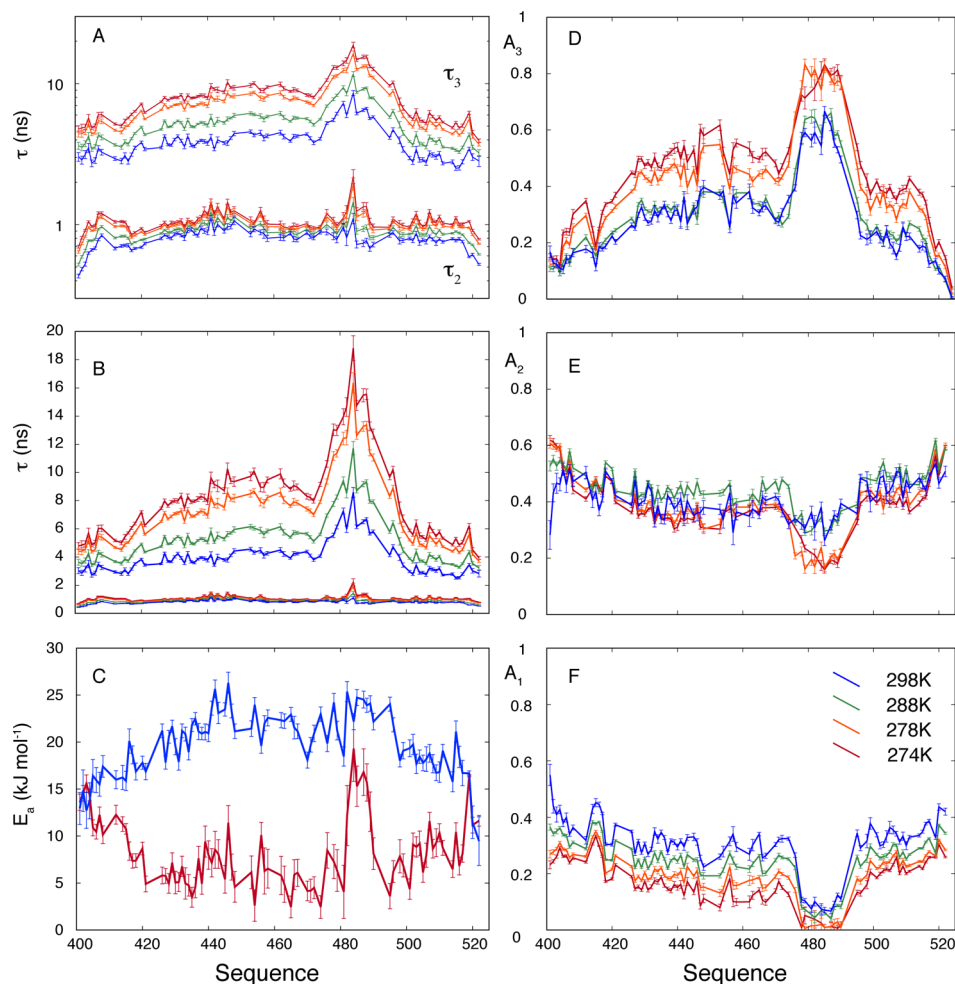
Figure 5. Simultaneous analysis of relaxation data measured over a range (274−298 K) using a site specific Arrhenius type relationship to model the characteristic correlation times of intermediate and slow motional modes in NT_L. (A, B) Intermediate (τ_2) and slow (τ_3) correlation times at 298 K (blue), 288 K (green), 278 K (orange), and 274 K (red). τ_3 exhibits a clear bell-shaped distribution, while τ_2 is much flatter over the sequence. The same data are shown in both plots, in (A) a logarithmic scale is used. (C) Effective activation energies describing the temperature coefficient of the motional time scales for each amino acid. Blue and red curves show the temperature coefficients of the slow (τ_3), and intermediate (τ_2) components, respectively. (D−F) Amplitude of the motional contributions A_3 (D, slowest contribution) A_2 (E, intermediate time scale contribution) and A_1 (F, fast contribution) at the four temperatures (color scheme as that in A, B). Error bars in all fits are derived from 200 noise based Monte Carlo simulations. Figure S11 shows the same fitting procedure applied to data from five temperatures simultaneously (268−298 K).

strengths by repeating the analysis with all data removed (at all temperatures) for each magnetic field strength independently. Time scales, amplitudes, and effective activation energies determined from only three fields reproduce values determined from the full analysis remarkably well, irrespective of the field that is removed from the analysis (Figure S14). Data from the removed field strength are again accurately predicted (Figure 6B) by the analysis using only three fields (Pearson's correlation coefficient $r > 0.996$ in all cases). This robustness is also remarkable because, in the latter case, up to 31% of the data are removed compared to the original analysis.

Dependence of Relaxation Rates on Chain Length. To investigate the segmental, or chain-like, motions further we have measured relaxation rates for two shorter constructs of the protein, lacking the first 43 amino acids (NT_M), and the first 43 and the last 23 amino acids respectively (NT_S) compared to the full length (NT_L). Typical rates measured at 278 K are compared in Figure 7, showing strong similarity between rates in constructs with common termini, from the helical region to the C-terminus in NT_M and NT_L and from the N-terminus to

the helical region in NT_S and NT_M. Applying the same motional model to data sets measured at 278 K for all three constructs (10 rates for NT_S, 12 rates for NT_M, and 14 rates for NT_L, Figure 8) reveals a similar distribution of the different amplitudes in the common regions of NT_S, NT_M, and NT_L, in particular in the helical element, accompanied by a close reproduction of the intermediate time scale motion τ_2. The slower motional time scale τ_3 exhibits a clear length-dependence on the helical element, with NT_L displaying the slowest motions and NT_S showing components that are approximately 5 ns faster than the same residues in NT_L. Although error bars are large, the data consistently show the same features throughout the helical element.

■ **DISCUSSION**

The dynamic modes and time scales sampled by intrinsically disordered proteins (IDPs) define their physical nature and therefore their activity. For this reason the establishment of a framework to describe the conformational dynamics of IDPs remains a key challenge for understanding their mechanistic
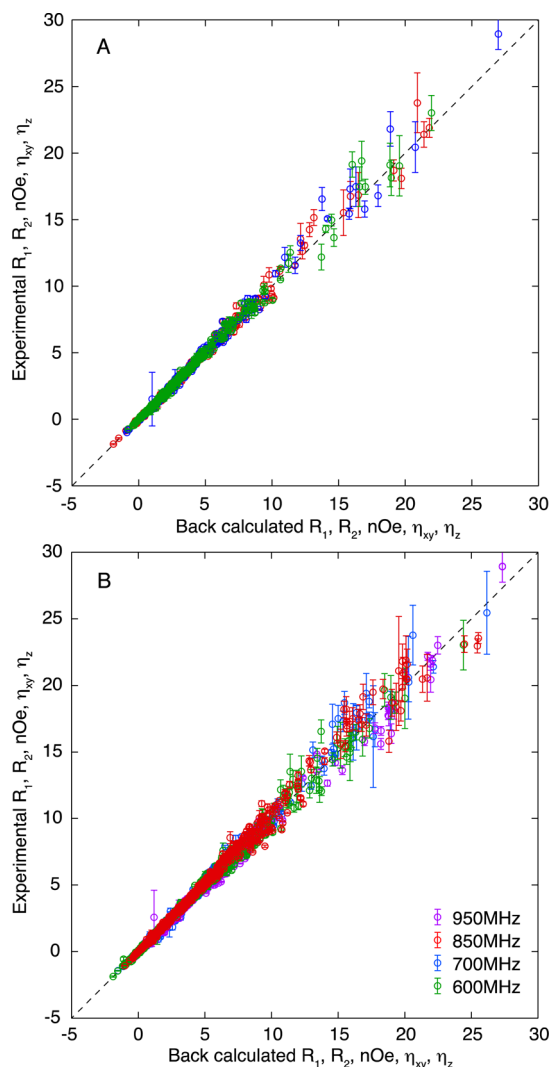
Figure 6. Cross-validation of the Arrhenius analysis of the multifield/multitemperature relaxation data. (A) Reproduction of experimental relaxation rates/enhancements using a cross-validation approach whereby 10% of all data were randomly removed and predicted from an Arrhenius analysis treating only the remaining 90%. Three random selections were performed, and results from all three are shown for the points removed in each case (red, green, and blue circles, $r > 0.995$ in all cases). Sequence dependence is shown in Figure S13. (B) Reproduction of experimental relaxation rates/enhancements using a cross-validation approach whereby all data points from each magnetic field strength (green, 600 MHz comprising 1230 relaxation measurements; blue, 700 MHz comprising 1402 relaxation measurements; red, 850 MHz comprising 1480 relaxation measurements; purple, 950 MHz comprising 787 relaxation measurements) were independently removed from the analysis and predicted from the fit of the remaining data using the Arrhenius analysis. $r > 0.996$ in all cases. Time scales, amplitudes, and effective activation energies derived from these analyses are very similar to those from the analysis using all available data (Figure S14).

and functional behavior. Although NMR relaxation represents the most accessible atomic resolution probe of protein dynamics, the assignment of the physical origin of the observed relaxation rates in IDPs remains obscure. In this study we have measured an extensive set of auto- and cross-correlated relaxation rates that offer complementary probes of different combinations of $J(\omega)$. These parameters were measured at multiple temperatures, thereby providing access to parameters
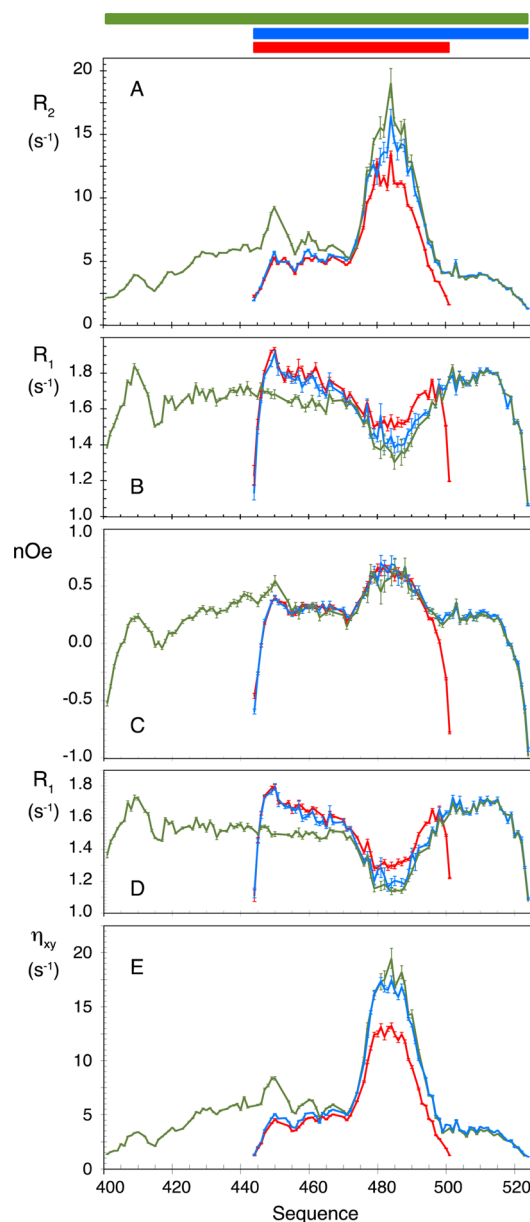

Figure 7. Length dependence of relaxation in NT. Comparison of representative relaxation rates measured at 278 K for NT_L (residues 401−524, green lines) NT_M (residues 444−524, blue lines) and NT_S (residues 444−501, red lines). (A) R_2 measured at 600 MHz. (B) R_1 measured at 600 MHz. (C) Heteronuclear NOE measured at 600 MHz. (D) R_1 measured at 700 MHz. (E) η_{xy} measured at 700 MHz.

that are sensitive, not only to kinetics, but also to the thermodynamic origin of the motions. Analysis of NT_L data measured at individual temperatures demonstrates that three independent contributions to the spectral density function are necessary to reproduce the experimental data. The time scale of the fastest component (characterized by τ_1) shows essentially no temperature dependence (Figure 3), with a pervasive contribution around 50 ps throughout the protein, except for the helical element where the fastest component is too fast to be determined. Lowering the temperature reduces the efficiency of relaxation from faster motions. The evolution of the parameters describing motion on time scales characterized by the intermediate (τ_2) and slow (τ_3) components is more complex, and in order to better understand this evolution we
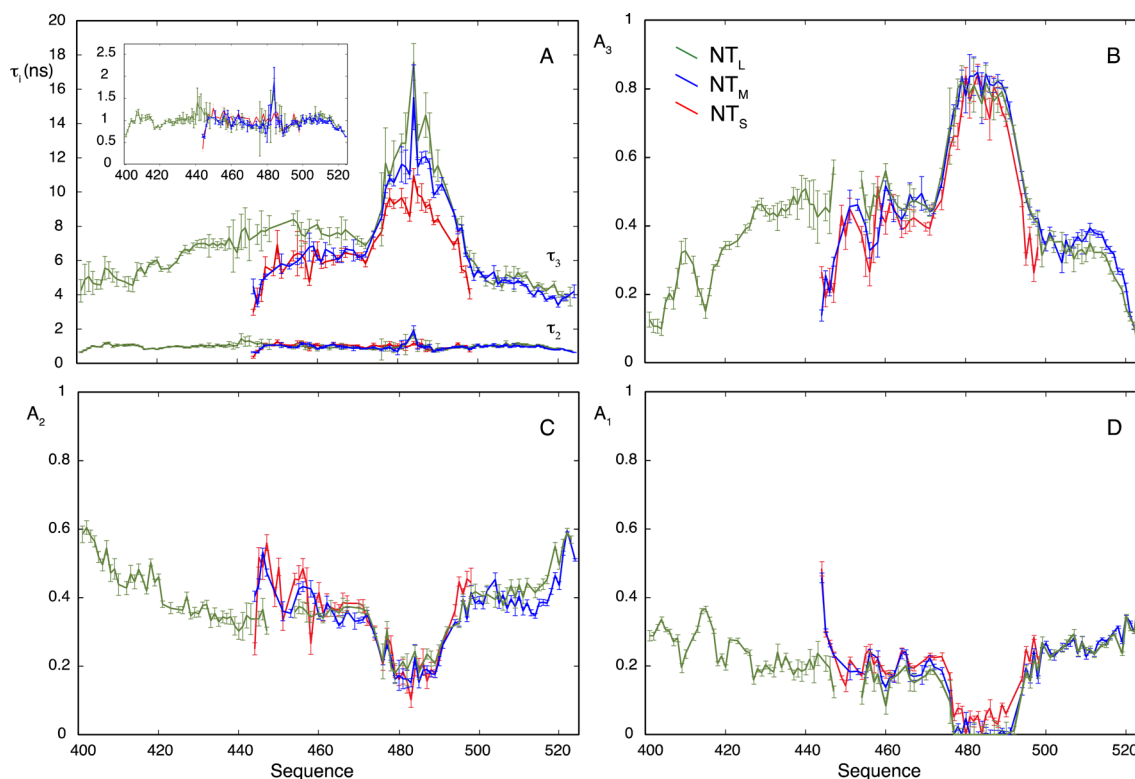
Figure 8. Comparison of the motional characterization of relaxation data measured for NT_L (green), NT_M (blue), and NT_S (red) with the three-exponential model of the autocorrelation function using the model-free approach at 278 K. (A) Characteristic intermediate (τ_2) and slow (τ_3) correlation times as a function of sequence. Inset shows only (τ_2) on a logarithmic scale. Error bars are derived from 200 noise based Monte Carlo simulations. (B–D) Amplitude of the motional contributions A_3 (B), A_2 (C), and A_1 (D) for the three chain lengths (color scheme as in A). Error bars again are derived from 200 noise based Monte Carlo simulations.

have simultaneously analyzed data for all temperatures at each site in the protein.

Site-specific Arrhenius analysis convincingly reproduces all 58 rates using only 13 fitted parameters (Figure S9) and provides considerable insight into the evolution of the different contributions. Remarkable correlation is seen between the amplitudes derived at the different temperatures (Figure 5). For example the GGG sequence at residue 415 shows increased amplitude fast motions (A_1), and the region between residue 424 and 438 exhibits a clear oscillation of contributions from both fast and intermediate time scale components (A_1, A_2) along the sequence (Figure 5E,F). This stretch corresponds to the primary sequence [424]ADIDLETEAHADQDA[438], where a repetitive alternation between hydrophobic and charged side chains dominates. The distribution of charged side chains, and their effect on the dynamics and function of IDPs, is a subject of current interest.[85] Here we appear to detect dynamic behavior that depends directly on the composition of the primary sequence.

In order to assess the stability of the approach, it is important to determine how accurately the model can predict independent data. This kind of cross-validation is rarely applied to spin relaxation measured in proteins; however, in view of the volume of available data at our disposal it is possible to rigorously apply such approaches, allowing us to estimate the predictive nature of the approach. The simultaneous Arrhenius analysis is shown to be remarkably robust with respect to removal of data and their back-prediction from fits to the remaining data points (Figure 6), both for random selections of

data and the entire removal of data from any single magnetic field (up to 31% of the total data set).

The Arrhenius analysis clearly separates slow and intermediate time scale contributions on the basis of their effective activation energies (Figure 5C). The slower time scale motion exhibits the strongest temperature dependence that coincides with expected values for viscosity-dominated rotational diffusion (Figure S12) and is consistently bell-shaped with respect to both time scale (Figure 5A,B) and contribution to the spectral density function (A_3) (Figure 5D). The intermediate time scale motions sample a more restricted range around 0.5–1.5 ns, which account for approximately 50% of the angular decorrelation in the disordered regions (Figure 5E), and are much flatter across the protein at all five temperatures, with the exception of the helical element. Intriguingly, in all nonhelical regions, A_2 exhibits a clear maximum at 288 K.

Putting these observations together, we can develop the following description. The fastest motional contribution occurs on a time scale of tens of picoseconds and exhibits negligible temperature dependence. These motions appear to be essentially librational, reporting on diffusion in an effectively flat potential, whose geometric limits apparently increase with increasing temperature, but which contains no detectable conformational energy barrier.

The flatness of both time scale and amplitude of the intermediate motions over the primary sequence, with the exception of the helical element and the termini, suggests that this component is largely independent of the chain-like nature of the protein and rather reports on local backbone sampling

dictated by the amino acid of interest and its immediate neighbors. The sequence-dependent activation energies of the intermediate time scale contribution fall in the range of around 5 kJ mol^{-1}, which coincides with values derived from both theoretical and UV-based studies of the free energy landscape of polypeptides.[86,87] Based on theoretically expected barriers between substrates (on the order of 15−20 kJ mol^{-1}),[32,34] our observations appear to report on diffusion within distinct Ramachandran minima (e.g., α-helical, polyproline II, β-strand) in the central part of the protein (420−510). Within 15 amino acids of the termini, values gradually increase. It seems likely that this reflects more complex sampling of the backbone in the presence of increased degrees of freedom at the chain termini. How exactly this impacts the effective activation energy of nanosecond motions is not clear and will probably require the use of MD simulation to propose a molecular origin of the phenomenon. The increase in $E_{a,2}$ is accompanied by a reduction in $E_{a,3}$ at both N- and C-termini, which becomes most noticeable beyond ^{414}GGG^{416} and ^{520}AG^{521}, suggesting that the phenomenon reports on segments of the chain that are gradually decoupled from the rest of the chain, until $E_{a,2}$ and $E_{a,3}$ converge at the termini, indicating that when the observed site is no longer part of a segmental chain, the two distinct contributions are no longer necessary. Importantly, the activation energy of the intermediate motions increases abruptly from 5 to 15−20 kJ mol^{-1} in the helical region, probably due to the increased conformational restriction in the helix, with higher activation energies associated with partial unfolding or constrained motion within the secondary structural element.[88,32,89,34] The average activation energies of backbone dynamics in a folded crystalline protein[64] that would be expected to be higher than those in a fluctuating helix in an IDP, were assigned values around 30 kJ mol^{-1}, placing the currently estimated values in the expected range.

Finally the slowest time scale component is assigned to segmental or chain-like motions: the dynamic parameters are bell-shaped, indicating a stronger dependence on segments and longer persistence lengths. The temperature dependence reproduces expected solvent viscosity behavior. End-effects extend to around 15 amino acids from the termini, supporting the idea that the slower component mainly reflects segmental motions within which modes are coupled, both to local residues and to the immediate solvation shell. In the helical element we observe a small but systematic dependence of the time scale of this component on construct length (Figure 8), while all other descriptors remain the same. It seems likely that this effect is only visible in the helical regions and not elsewhere, because the autocorrelation functions in the unfolded regions are more efficiently quenched by extensive faster time scale motions. The viscosity-dominated drag effect is probably related to the observation of longer effective rotational correlation times of folded domains when disordered domains are present, making them apparently more "sluggish" in solution.[59]

The sensitivity of spin relaxation to slower motions in IDPs is entirely dependent on the efficiency of fast motions to quench the angular correlation function, so that in the helix, where this sensitivity is maximal, it is possible to detect motions as slow as 20 ns at 274 K (and 25 ns at 268 K). In this respect, engineering short stable helices into long IDPs may provide a sensitive approach to the detection of such slower motions. These considerations are also important for example for the study of relaxation of IDPs in more complex environments, where slower chain-like motions may affect effective relaxation

characteristics of prestructured linear motifs, even in the absence of direct interaction with partner proteins.

■ CONCLUSIONS

In conclusion, the measurement of an extensive set of relaxation rates not only at multiple magnetic fields but also at multiple temperatures and in three different length constructs of the same IDP has allowed us to characterize the dynamic nature of SeV NT in unprecedented detail. Simultaneous analysis of up to 61 relaxation rates per amino acid assigns local activation energies along the chain and identifies three physically distinct dynamic modes, reporting on librational motions, local backbone sampling, and chain motions. The analysis is shown to be statistically highly robust and to accurately predict relaxation data measured at different magnetic field strengths and temperatures, providing a novel framework for the description of the dynamic properties of IDPs. The ability to identify intrinsic modes and time scales at atomic resolution from NMR spin relaxation will contribute significantly to our understanding of the behavior and function of IDPs, while providing a new and essential dimension to our description of this biologically important and ubiquitous class of proteins.

■ EXPERIMENTAL SECTION

Sample Preparation. Three constructs of the NT domain, comprising residues 401−524 (NT$_L$), 444−524 (NT$_M$), and 444−501 (NT$_S$) of the nucleoprotein of Sendai virus strain Harris, whose sequence corresponds to that of SeV Fushimi strain NT (UniProtKB accession number Q07097) except for mutation E410 K, were expressed and purified as described previously.[63,77] NMR was performed at protein concentrations of 500 μM in 50 mM sodium phosphate buffer at pH 6.0 with 500 mM NaCl containing 10% D$_2$O (v/v).

NMR Spectroscopy. The assignment of the longest construct of NT (residues 401−524) was obtained at 298 K using a set of six BEST-type triple resonance[90] correlating Cα, Cβ, and C′ acquired on a Varian spectrometer operating at a ^{1}H frequency of 600 MHz. Spectra were processed in NMRPipe[91] and analyzed in Sparky,[92] and MARS[93] was used to obtain sequential connectivities. The assignment of this construct was also obtained at 278 K using similar experiments and procedures. The assignments at 298 K of the shorter constructs of NT were obtained previously.[63,77]

NMR relaxation experiments were performed on Bruker spectrometers operating at ^{1}H frequencies of 600, 700, 850, and 950 MHz. Relaxation rates were measured for NT$_L$, NT$_M$, and NT$_S$, in identical buffer, at 298, 288, 278, 274, and 268 K. Spectral assignments at temperatures between 278 and 298 K were obtained by following the evolution of ^{1}H−^{15}N HSQC spectra with temperature (steps of 5 K). ^{15}N longitudinal relaxation (R_1) and {^{1}H}-^{15}N heteronuclear NOE and $R_{1\rho}$ (using a spin lock of 1.5 kHz) were measured as described by Lakomek et al.[94] ^{15}N transverse relaxation (R_2) was determined from $R_{1\rho}$ and R_1, taking into account resonance offset.[95] ^{15}N−^{1}H CSA/DD cross-correlated transverse (η_{xy}) and longitudinal (η_z) relaxation rates were measured as described by Pelupessy et al.[96,97]

An interscan delay of 1.5−3 s and 64−128 dummy scans were used for measuring $R_{1\rho}$, R_1, η_{xy}, and η_z rates. The typical set of relaxation delays included [1, 20, 50, 70, 90, 130, 170, 210, 230] ms for $R_{1\rho}$ experiments and [0, 0.6, 0.08, 1.6, 0.4, 1.8, 1.04, 0.8, 0.2, 0.6] s for the R_1 experiment. Shorter delays, [1, 10, 20, 35, 50, 70, 90, 120] ms, were used for measuring the $R_{1\rho}$ relaxation rate at 268 K. For η_{xy} and η_z relaxation delays of 50 and 100 ms were used, respectively.

Temperature was individually calibrated on each spectrometer using a 99.8% methanol-d_4 sample by measuring the chemical shift difference $\Delta\delta$ between OH and CH$_2$ peaks in the ^{1}H spectrum and using the following equation:

$$T = -16.7467 \cdot (\Delta\delta)^2 - 52.5130 \cdot \Delta\delta + 419.1381 \qquad (9)$$

where $\Delta\delta$ is the chemical shift difference in ppm. Significant sample heating during the relaxation experiments was excluded by monitoring the position of the cross peaks.

All spectra were processed in NMRPipe[91] and analyzed in CCPN.[98] The data set measured at supercooled temperatures (268 K) was obtained by employing 3 mm NMR tubes. The high salt concentration (500 mM) prevents the solution from freezing at this temperature.

Fitting Procedure. A Levenberg−Marquardt algorithm was used to fit the data to the expressions in eqs 1−8 using the definition of the spectral density function in eq 7, by minimizing the following function for each residue i:

$$\chi_i^2 = \sum_{n=1}^{5} \sum_{m=1}^{N} \left\{ \frac{(R_{n,\text{expt}}^m - R_{n,\text{calcd}}^m)}{\sigma_{n,\text{expt}}^m} \right\}^2 \tag{10}$$

where n identifies the different rates and m identifies the different temperatures used in the fit (one, four, or five temperatures). When only one temperature is considered, $(\tau_1, \tau_2, A_2,$ and $\theta)$, $(A_2, A_3, \tau_1, \tau_2, \tau_3,$ and $\theta)$, or $(A_2, A_3, \tau_2, \tau_3,$ and $\theta)$ were optimized using a nonlinear least-squares fitting approach. When multiple temperatures are analyzed simultaneously, A_2 and A_3 are optimized for each temperature, together with $\tau_{2,\infty}, \tau_{3,\infty}, E_{a,2}, E_{a,3},$ and θ.

Several models were tested when analyzing relaxation at each temperature: a model containing three motional time scales with six fitting parameters $(A_2, A_3, \tau_1, \tau_2, \tau_3,$ and the angle θ; $A_1 = 1 - A_2 - A_3)$; a model with three motional time scales in which τ_1 was either fixed at 50 ps (for the unfolded chain) or set to 0 (for the helical region), resulting in five parameters $(A_2, A_3, \tau_2, \tau_3,$ and $\theta)$; a model with two motional modes and four parameters $(\tau_2, \tau_3, A_3,$ and θ, while $A_2 = 1 - A_3)$, and finally a model with one motional mode and two parameters $(\tau$ and $\theta)$.

Statistical Analysis. Errors were estimated using explicit noise-based Monte Carlo simulations in all cases. The results were concordant. Experimental errors were estimated from repeat measurements. In the case of data from 298 and 278 K, experimental errors were scaled by a factor of 1.4, so that the total target function for each individual temperature was within 95% confidence limits. The results of the fit to different models were compared using the corrected Akaike Information Criterion.[99]

ASSOCIATED CONTENT

Ⓢ Supporting Information

The Supporting Information is available free of charge on the ACS Publications website at DOI: 10.1021/jacs.6b02424.

Supporting figures showing comparison of secondary structure as a function of temperature, relaxation rates measured at 268 K, results of reduced spectral density mapping, statistical analysis of model-free treatment, three-component analysis with variable τ_1, analysis of θ as a function of sequence, Arrhenius analysis of data from 268 to 298 K, viscosity dependence of 500 mM saline solution as a function of temperature (PDF)

AUTHOR INFORMATION

Corresponding Author

*martin.blackledge@ibs.fr

Present Address

†Université Lille 1, UMR CNRS 8576, 50 avenue du Halley, 59650 Villeneuve d'Ascq, France.

Author Contributions

‡A.A. and N.S. contributed equally.

Notes

The authors declare no competing financial interest.

REFERENCES

(1) Uversky, V. N. *Protein Sci.* **2002**, *11*, 739−756.
(2) Dyson, H. J.; Wright, P. E. *Nat. Rev. Mol. Cell Biol.* **2005**, *6*, 197−208.
(3) Tompa, P.; Davey, N. E.; Gibson, T. J.; Babu, M. M. *Mol. Cell* **2014**, *55*, 161−169.
(4) Dyson, H. J.; Wright, P. E. *Chem. Rev.* **2004**, *104*, 3607−3622.
(5) Forman-Kay, J. D.; Mittag, T. *Structure* **2013**, *21*, 1492−1499.
(6) Jensen, M. R.; Ruigrok, R. W.; Blackledge, M. *Curr. Opin. Struct. Biol.* **2013**, *23*, 426−435.
(7) Rezaei-Ghaleh, N.; Blackledge, M.; Zweckstetter, M. *ChemBioChem* **2012**, *13*, 930−950.
(8) Sgourakis, N. G.; Yan, Y.; McCallum, S. A.; Wang, C.; Garcia, A. E. *J. Mol. Biol.* **2007**, *368*, 1448−1457.
(9) Wu, K.-P.; Weinstock, D. S.; Narayanan, C.; Levy, R. M.; Baum, J. *J. Mol. Biol.* **2009**, *391*, 784−796.
(10) Zhang, W.; Ganguly, D.; Chen, J. *PLoS Comput. Biol.* **2012**, *8*, e1002353.
(11) Narayanan, C.; Weinstock, D. S.; Wu, K.-P.; Baum, J.; Levy, R. M. *J. Chem. Theory Comput.* **2012**, *8*, 3929−3942.
(12) Mittal, J.; Yoo, T. H.; Georgiou, G.; Truskett, T. M. *J. Phys. Chem. B* **2013**, *117*, 118−124.
(13) Marsh, J. A.; Forman-Kay, J. D. *J. Mol. Biol.* **2009**, *391*, 359−374.
(14) Salmon, L.; Nodet, G.; Ozenne, V.; Yin, G.; Jensen, M. R.; Zweckstetter, M.; Blackledge, M. *J. Am. Chem. Soc.* **2010**, *132*, 8407−8418.
(15) Fisher, C. K.; Huang, A.; Stultz, C. M. *J. Am. Chem. Soc.* **2010**, *132*, 14919−14927.
(16) Jensen, M. R.; Zweckstetter, M.; Huang, J.; Blackledge, M. *Chem. Rev.* **2014**, *114*, 6632−6660.
(17) Jensen, M. R.; Blackledge, M. *Proc. Natl. Acad. Sci. U. S. A.* **2014**, *111*, E1557−1558.
(18) Csermely, P.; Palotai, R.; Nussinov, R. *Trends Biochem. Sci.* **2010**, *35*, 539−546.
(19) Wright, P. E.; Dyson, H. J. *Curr. Opin. Struct. Biol.* **2009**, *19*, 31−38.
(20) Sugase, K.; Dyson, H. J.; Wright, P. E. *Nature* **2007**, *447*, 1021−1025.
(21) Hilser, V. J.; Thompson, E. B. *Proc. Natl. Acad. Sci. U. S. A.* **2007**, *104*, 8311−8315.
(22) Kiefhaber, T.; Bachmann, A.; Jensen, K. S. *Curr. Opin. Struct. Biol.* **2012**, *22*, 21−29.
(23) Iesmantavicius, V.; Dogan, J.; Jemth, P.; Teilum, K.; Kjaergaard, M. *Angew. Chem., Int. Ed.* **2014**, *53*, 1548−1551.
(24) Rogers, J. M.; Wong, C. T.; Clarke, J. *J. Am. Chem. Soc.* **2014**, *136*, 5197−5200.
(25) Schneider, R.; Maurin, D.; Communie, G.; Kragelj, J.; Hansen, D. F.; Ruigrok, R. W. H.; Jensen, M. R.; Blackledge, M. *J. Am. Chem. Soc.* **2015**, *137*, 1220−1229.
(26) Gianni, S.; Dogan, J.; Jemth, P. *Curr. Opin. Struct. Biol.* **2016**, *36*, 18−24.
(27) Shoemaker, B. A.; Portman, J. J.; Wolynes, P. G. *Proc. Natl. Acad. Sci. U. S. A.* **2000**, *97*, 8868−8873.

(28) Fawzi, N. L.; Phillips, A. H.; Ruscio, J. Z.; Doucleff, M.; Wemmer, D. E.; Head-Gordon, T. *J. Am. Chem. Soc.* **2008**, *130*, 6145−6158.

(29) Lindorff-Larsen, K.; Trbovic, N.; Maragakis, P.; Piana, S.; Shaw, D. E. *J. Am. Chem. Soc.* **2012**, *134*, 3787−3791.

(30) Robustelli, P.; Trbovic, N.; Friesner, R. A.; Palmer, A. G. *J. Chem. Theory Comput.* **2013**, *9*, 5190−5200.

(31) Vitalis, A.; Pappu, R. V. *J. Comput. Chem.* **2009**, *30*, 673−699.

(32) Best, R. B.; Hummer, G. *J. Phys. Chem. B* **2009**, *113*, 9004−9015.

(33) Piana, S.; Donchev, A. G.; Robustelli, P.; Shaw, D. E. *J. Phys. Chem. B* **2015**, *119*, 5113−5123.

(34) Rauscher, S.; Gapsys, V.; Gajda, M. J.; Zweckstetter, M.; de Groot, B. L.; Grubmüller, H. *J. Chem. Theory Comput.* **2015**, *11*, 5513−5524.

(35) Palmer, A. *Chem. Rev.* **2004**, *104*, 3623−3640.

(36) Alexandrescu, A.; Shortlet, D. *J. Mol. Biol.* **1994**, *242*, 527−546.

(37) Farrow, N.; Zhang, O.; Formankay, J.; Kay, L. *Biochemistry* **1995**, *34*, 868−878.

(38) Frank, M.; Clore, G.; Gronenborn, A. *Protein Sci.* **1995**, *4*, 2605−2615.

(39) Brutscher, B.; Brüschweiler, R.; Ernst, R. R. *Biochemistry* **1997**, *36*, 13043−13053.

(40) Schwalbe, H.; Fiebig, K. M.; Buck, M.; Jones, J. A.; Grimshaw, S. B.; Spencer, A.; Glaser, S. J.; Smith, L. J.; Dobson, C. M. *Biochemistry* **1997**, *36*, 8977−8991.

(41) Buevich, A. V.; Baum, J. *J. Am. Chem. Soc.* **1999**, *121*, 8671−8672.

(42) Yang, D. W.; Mok, Y. K.; Muhandiram, D. R.; Forman-Kay, J. D.; Kay, L. E. *J. Am. Chem. Soc.* **1999**, *121*, 3555−3556.

(43) Yao, J.; Chung, J.; Eliezer, D.; Wright, P. E.; Dyson, H. J. *Biochemistry* **2001**, *40*, 3561−3571.

(44) Ochsenbein, F.; Neumann, J. M.; Guittet, E.; Van Heijenoort, C. *Protein Sci.* **2002**, *11*, 957−964.

(45) Klein-Seetharaman, J.; Oikawa, M.; Grimshaw, S. B.; Wirmer, J.; Duchardt, E.; Ueda, T.; Imoto, T.; Smith, L. J.; Dobson, C. M.; Schwalbe, H. *Science* **2002**, *295*, 1719−1722.

(46) Yang, D. W.; Kay, L. E. *J. Mol. Biol.* **1996**, *263*, 369−382.

(47) Wirmer, J.; Peti, W.; Schwalbe, H. *J. Biomol. NMR* **2006**, *35*, 175−186.

(48) Le Duff, C. S.; Whittaker, S. B.-M.; Radford, S. E.; Moore, G. R. *J. Mol. Biol.* **2006**, *364*, 824−835.

(49) Houben, K.; Blanchard, L.; Blackledge, M.; Marion, D. *Biophys. J.* **2007**, *93*, 2830−2844.

(50) Ebert, M.-O.; Bae, S.-H.; Dyson, H. J.; Wright, P. E. *Biochemistry* **2008**, *47*, 1299−1308.

(51) Modig, K.; Poulsen, F. M. *J. Biomol. NMR* **2008**, *42*, 163−177.

(52) Silvers, R.; Sziegat, F.; Tachibana, H.; Segawa, S.; Whittaker, S.; Günther, U. L.; Gabel, F.; Huang, J.; Blackledge, M.; Wirmer-Bartoschek, J.; Schwalbe, H. *J. Am. Chem. Soc.* **2012**, *134*, 6846−6854.

(53) Sziegat, F.; Silvers, R.; Hähnke, M.; Jensen, M. R.; Blackledge, M.; Wirmer-Bartoschek, J.; Schwalbe, H. *Biochemistry* **2012**, *51*, 3361−3372.

(54) Kurzbach, D.; Schwarz, T. C.; Platzer, G.; Hoefler, S.; Hinderberger, D.; Konrat, R. *Angew. Chem., Int. Ed.* **2014**, *53*, 3840−3843.

(55) Cho, M.-K.; Kim, H.-Y.; Bernado, P.; Fernandez, C. O.; Blackledge, M.; Zweckstetter, M. *J. Am. Chem. Soc.* **2007**, *129*, 3032−3033.

(56) Bussell, R.; Eliezer, D. *J. Biol. Chem.* **2001**, *276*, 45996−46003.

(57) Bertoncini, C. W.; Jung, Y.-S.; Fernandez, C. O.; Hoyer, W.; Griesinger, C.; Jovin, T. M.; Zweckstetter, M. *Proc. Natl. Acad. Sci. U. S. A.* **2005**, *102*, 1430−1435.

(58) Parigi, G.; Rezaei-Ghaleh, N.; Giachetti, A.; Becker, S.; Fernandez, C.; Blackledge, M.; Griesinger, C.; Zweckstetter, M.; Luchinat, C. *J. Am. Chem. Soc.* **2014**, *136*, 16201−16209.

(59) Bae, S.-H.; Dyson, H. J.; Wright, P. E. *J. Am. Chem. Soc.* **2009**, *131*, 6814−6821.

(60) Amoros, D.; Ortega, A.; Garcia de la Torre, J. *J. Chem. Theory Comput.* **2013**, *9*, 1678−1685.

(61) Rezaei-Ghaleh, N.; Klama, F.; Munari, F.; Zweckstetter, M. *Angew. Chem., Int. Ed.* **2013**, *52*, 11410−11414.

(62) Blanchard, L.; Tarbouriech, N.; Blackledge, M.; Timmins, P.; Burmeister, W. P.; Ruigrok, R. W. H.; Marion, D. *Virology* **2004**, *319*, 201−211.

(63) Houben, K.; Marion, D.; Tarbouriech, N.; Ruigrok, R. W. H.; Blanchard, L. *J. Virol.* **2007**, *81*, 6807−6816.

(64) Lewandowski, J. R.; Halse, M. E.; Blackledge, M.; Emsley, L. *Science* **2015**, *348*, 578−581.

(65) Peng, J. W.; Wagner, G. *Biochemistry* **1992**, *31*, 8571−8586.

(66) Farrow, N.; Zhang, O.; Szabo, A.; Torchia, D.; Kay, L. *J. Biomol. NMR* **1995**, *6*, 153−162.

(67) Ishima, R.; Nagayama, K. *Biochemistry* **1995**, *34*, 3162−3171.

(68) Kaderavek, P.; Zapletal, V.; Rabatinova, A.; Krasny, L.; Sklenar, V.; Zidek, L. *J. Biomol. NMR* **2014**, *58*, 193−207.

(69) Halle, B.; Wennerström, H. *J. Chem. Phys.* **1981**, *75*, 1928−1943.

(70) Lipari, G.; Szabo, A. *J. Am. Chem. Soc.* **1982**, *104*, 4546−4559.

(71) Clore, G.; Szabo, A.; Bax, A.; Kay, L.; Driscoll, P.; Gronenborn, A. *J. Am. Chem. Soc.* **1990**, *112*, 4989−4991.

(72) Halle, B. *J. Chem. Phys.* **2009**, *131*, 224507.

(73) Cole, K. S.; Cole, R. H. *J. Chem. Phys.* **1941**, *9*, 341−351.

(74) Prompers, J. J.; Brüschweiler, R. *J. Am. Chem. Soc.* **2002**, *124*, 4522−4534.

(75) Khan, S. N.; Charlier, C.; Augustyniak, R.; Salvi, N.; Dejean, V.; Bodenhausen, G.; Lequin, O.; Pelupessy, P.; Ferrage, F. *Biophys. J.* **2015**, *109*, 988−999.

(76) Gill, M. L.; Byrd, R. A.; Arthur, G.; Palmer. *Phys. Chem. Chem. Phys.* **2016**, *18*, 5839−5849.

(77) Jensen, M. R.; Houben, K.; Lescop, E.; Blanchard, L.; Ruigrok, R. W. H.; Blackledge, M. *J. Am. Chem. Soc.* **2008**, *130*, 8055−8061.

(78) Jensen, M. R.; Blackledge, M. *J. Am. Chem. Soc.* **2008**, *130*, 11266−11267.

(79) de Alba, E.; Baber, J.; Tjandra, N. *J. Am. Chem. Soc.* **1999**, *121*, 4282−4283.

(80) Kjaergaard, M.; Brander, S.; Poulsen, F. M. *J. Biomol. NMR* **2011**, *49*, 139−149.

(81) Loth, K.; Pelupessy, P.; Bodenhausen, G. *J. Am. Chem. Soc.* **2005**, *127*, 6062−6068.

(82) Hall, J. B.; Fushman, D. *J. Am. Chem. Soc.* **2006**, *128*, 7855−7870.

(83) Yao, L.; Grishaev, A.; Cornilescu, G.; Bax, A. *J. Am. Chem. Soc.* **2010**, *132*, 4295−4309.

(84) Kestin, J.; Khalifa, H. E.; Correia, R. J. *J. Phys. Chem. Ref. Data* **1981**, *10*, 71−88.

(85) Das, R. K.; Pappu, R. V. *Proc. Natl. Acad. Sci. U. S. A.* **2013**, *110*, 13392−13397.

(86) Young, W. S.; Brooks, C. L., III *J. Mol. Biol.* **1996**, *259*, 560−572.

(87) Mikhonin, A. V.; Asher, S. A. *J. Am. Chem. Soc.* **2006**, *128*, 13789−13795.

(88) Huang, C.-Y.; Getahun, Z.; Zhu, Y.; Klemke, J. W.; DeGrado, W. F.; Gai, F. *Proc. Natl. Acad. Sci. U. S. A.* **2002**, *99*, 2788−2793.

(89) Best, R. B.; Mittal, J. *J. Phys. Chem. B* **2010**, *114*, 8790−8798.

(90) Lescop, E.; Schanda, P.; Brutscher, B. *J. Magn. Reson.* **2007**, *187*, 163−169.

(91) Delaglio, F.; Grzesiek, S.; Vuister, G. W.; Zhu, G.; Pfeifer, J.; Bax, A. *J. Biomol. NMR* **1995**, *6*, 277−293.

(92) Goddard, T.; Kneller, D. G. *SPARKY 3*; University of California—San Francisco.

(93) Jung, Y.-S.; Zweckstetter, M. *J. Biomol. NMR* **2004**, *30*, 11−23.

(94) Lakomek, N.-A.; Ying, J.; Bax, A. *J. Biomol. NMR* **2012**, *53*, 209−221.

(95) Akke, M.; Palmer, A. G. *J. Am. Chem. Soc.* **1996**, *118*, 911−912.

(96) Pelupessy, P.; Espallargas, G. M.; Bodenhausen, G. *J. Magn. Reson.* **2003**, *161*, 258−264.

(97) Pelupessy, P.; Ferrage, F.; Bodenhausen, G. *J. Chem. Phys.* **2007**, *126*, 134508.

(98) Vranken, W. F.; Boucher, W.; Stevens, T. J.; Fogh, R. H.; Pajon, A.; Llinas, M.; Ulrich, E. L.; Markley, J. L.; Ionides, J.; Laue, E. D. *Proteins: Struct., Funct., Genet.* **2005**, *59*, 687−696.

(99) Burnham, K. P.; Anderson, D. R. *Sociol. Methods Res.* **2004**, *33*, 261−304.